Received: 4 December 2022 | Revised: 8 June 2023 | Accepted: 11 June 2023 | Published on: 4 July 2023

DOI: 10.1002/qj.4511

Quarterly Journal of the Royal Meteorological Society RMetS

RESEARCH ARTICLE

Comparison of temperature and wind observations in the Tropics in a perfect-model, global EnKF data assimilation system

Lanqian Li[1,2] | **Nedjeljka Žagar**[1] | **Kevin Raeder**[3] | **Jeffrey L. Anderson**[3]

[1]Meteorological Institute, Center for Earth System Research and Sustainability, Universität Hamburg, Hamburg, Germany

[2]College of Atmospheric Science, Lanzhou University, Lanzhou, China

[3]Computational Information Systems Laboratory, National Center for Atmospheric Research, Boulder, Colorado, USA

Correspondence
Nedjeljka Žagar, Meteorological Institute, Universität Hamburg, Grindelberg 7, 20144 Hamburg, Germany.
Email: nedjeljka.zagar@uni-hamburg.de

Funding information
China Scholarship Council, Grant/Award Number: 202106180040; Deutsche Forschungsgemeinschaft, Grant/Award Number: 461186383

Flow-dependent errors in tropical analyses and short-range forecasts are analysed using global observing-system simulation experiments assimilating only temperature, only winds, and both data types using the ensemble Kalman filter (EnKF) Data Assimilation Research Testbed (DART) and a perfect model framework. The idealised, homogeneous observation network provides profiles of wind and temperature data from the nature run for January 2018 using the National Center for Atmospheric Research (NCAR) Community Earth System Model (CESM) forced by the observed sea-surface temperature. The results show that the assimilation of abundant wind observations in a perfect model makes the temperature data in the Tropics largely uninformative. Furthermore, the assimilation of wind data reduces the background errors in specific humidity twice as much as the assimilation of temperature observations. In all experiments, the largest analysis uncertainties and the largest short-term forecast errors are found in regions of strong vertical and longitudinal gradients in the background wind, especially in the upper troposphere and lower stratosphere over the Indian Ocean and Maritime Continent. The horizontal error correlation scales are on average short throughout the troposphere, just several hundred km. The correlation scales of the wind variables in precipitating regions are half of those in nonprecipitating regions. In precipitating regions, the correlations are elongated vertically, especially for the wind variables. Strong positive cross-correlations between temperature and specific humidity in the precipitating regions are explained using the Clausius–Clapeyron equation.

KEYWORDS
ensemble Kalman filter data assimilation, forecast-error correlations, mass and wind observations, temperature–moisture cross-correlations, Tropics

1 | INTRODUCTION

Outputs from numerical weather prediction (NWP) models have been improving continuously, thereby supporting societal adaptation to extreme events (Emerton *et al.*, 2022). Part of the forecast improvement comes from more accurate initial states for the NWP model forecasts, as a result of an increasing number of

observations, their better use in data assimilation, and a more accurate background field (also called the first guess or *prior*). For example, the data assimilation system of the European Centre for Medium-Range Weather Forecasts (ECMWF) currently assimilates observations from about 100 satellite instruments, which is about three times as many as 20 years ago. Additional satellite observations provide better coverage of the global atmosphere and include new types of observations such as radio occultation measurements (Healy *et al.*, 2020) and vertical wind profiles from *Aeolus*, the Doppler wind lidar measuring horizontal line-of-sight (HLOS) winds (Stoffelen *et al.*, 2005).

Launched in 2018, *Aeolus* provided, for the first time, global coverage of wind profiles. Despite their lower accuracy compared with conventional wind observations, HLOS wind profiles improved analyses and forecasts in all operational NWP models that assimilated the HLOS winds (Rennie *et al.*, 2021; Garrett *et al.*, 2022; Laroche and St-James, 2022; Pourret *et al.*, 2022). The largest improvements by *Aeolus* are seen in the tropical upper troposphere and lower stratosphere (UTLS), with *Aeolus* correcting both systematic and random errors (Rennie *et al.*, 2021). The present study aims to explain different effects of assimilating temperature and wind observations in the Tropics in relation to the background state in a perfect model.

The demonstrated impact of *Aeolus* corroborates the well-known fact that the wind-field information cannot be reconstructed easily from temperature observations in the Tropics (Gordon *et al.*, 1972), not even with four-dimensional variational (4DVar) data assimilation with a perfect model (Žagar *et al.*, 2004). This is commonly illustrated using geostrophic theory for the rotating shallow-water equations (e.g. Kalnay, 2003, Chapter 5.7). The associated linearised potential vorticity equation is

$$\frac{d}{dt}\left(\nabla^2\Psi + f - \frac{f_0}{gD}\phi\right) = 0, \tag{1}$$

where Ψ is the geostrophic stream function and ϕ is the geopotential perturbation from the mean value $\Phi = gD$, where D is the mean depth of the fluid layer and g is the gravity. The Coriolis parameter f is defined as $f = 2\Omega\sin(\varphi)$; its local value at latitude $\varphi = \varphi_0$ is denoted f_0, and Ω is the Earth rotation rate. The assumption of geostrophically balanced analysis increments in response to geopotential or wind observations leads to the conditions $K^2L_R^2 \gg 1$ and $K^2L_R^2 \ll 1$ for short or long scales, associated with greater usefulness of the wind and mass observations, respectively. Here, K denotes the horizontal wavenumber in (in m^{-1}), defined as $K^2 = k^2 + l^2$, where k and l are the zonal and meridional wavenumbers, respectively. The parameter $L_R = \sqrt{gD}/f_0$ is the external Rossby deformation radius (in m), the horizontal scale of the geostrophic balancing process on the f-plane for a given D and f_0. The wavelength $L = 2\pi/K$, which separates "long" and "short" horizontal wavelengths, is thus

$$L = 2\pi L_R = 2\pi\sqrt{gD}/f_0. \tag{2}$$

The shallow-water framework is a simple analogue of the complex baroclinic primitive equation model, in which case D would represent an equivalent depth and the third term of Equation 1 would include stratification. The wavelength L is shown in Figure 1 every 10° of latitude. For any φ, horizontal motions with length-scales to the right of and below the curve are represented better by mass-field than by wind-field observations. In other words, for these scales the solution of the initialization problem for our simple system retains information provided by the mass data.

How long are the scales at which mass-field information has a greater value than wind data? Answering this question in high latitudes (large φ) requires careful consideration, due to spherical geometry. This is illustrated in Figure 1 by comparing the wavelength L with the maximal resolvable wavelength at the local circumference $R = 2\pi a\cos(\varphi)$, a being the Earth radius, at every latitude

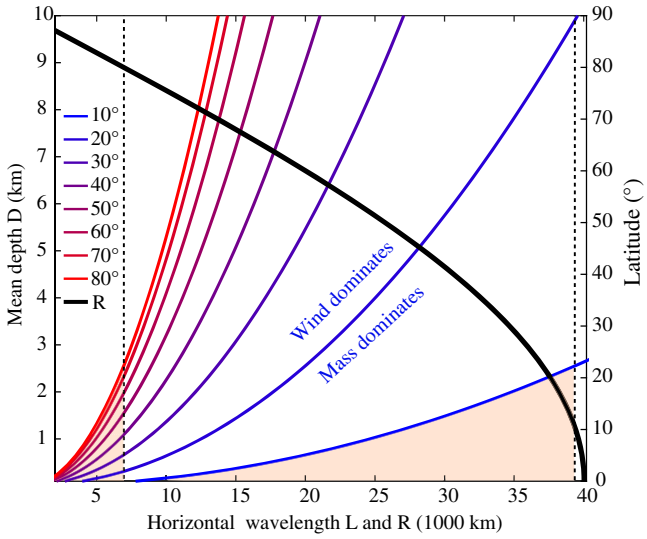

FIGURE 1 Horizontal wavelength L defined by Equation 2 as a function of the mean fluid depth D for several latitudes φ (in degrees, as shown in the legend). The bottom curve is for $\varphi = 10°$ and the leftmost curve is for $\varphi = 80°$. For every $L(\varphi)$, wind-field information is more useful than geopotential data on the left and above the curve. The thick curve is the Earth circumference R as a function of latitude shown on the right-hand y-axis. For every φ, only wavelengths shorter than R should be discussed. The two shaded areas are (L, D) regions where mass-field information is more useful than wind data at 80° and at 10°. [Colour figure can be viewed at wileyonlinelibrary.com]

(black curve). Latitudes are shown on the right y-axis in Figure 1. Only solutions for $L < R$ can be interpreted in Figure 1. For example, at $\varphi = 80°$, $R = 6.95 \times 10^3$ km and quasigeostrophic theory suggests that mass-field information is more useful only for vertical depths $D < 2.5$ km (shaded region). In other words, flows with significant vertical depth in the polar regions are constrained better by wind-field information. Moving equatorward, values of L grow larger. At 20° and $D = 10$ km, the wavelength $L \approx 39.4 \times 10^3$ km exceeds the circumference $R \approx 37.6 \times 10^3$ km. Figure 1 suggests that, for most depths and scales in the Tropics, direct wind information is more informative than mass data. In other words, the linear balance equation is of little value in the Tropics (Daley, 1991, Chapter 7).

Within the Tropics, the horizontal flows become largely anisotropic. The quasigeostrophic framework used to derive Equation 2 no longer applies and the Rossby deformation radius is replaced by the equatorial radius of deformation $(\sqrt{gD}/2\beta)^{1/2}$, where $\beta = \partial f/\partial y = a^{-1}\partial f/\partial\varphi$. The initialisation must consider large-scale divergent flows such as equatorial Kelvin and mixed Rossby–gravity waves, which are associated with a significant part of day-to-day circulation variability (e.g. Kiladis *et al.*, 2009) and are a significant contributor to the growth of forecast errors in the Tropics (e.g. Žagar *et al.*, 2015). This has presented a problem for three-dimensional variational (3DVar) data assimilation schemes, which traditionally have focused on the errors in the quasigeostrophic flow in the extratropics (Derber, 1987). In that approach, the wind field is a sum of balanced and unbalanced components. The balanced part is obtained from the geopotential field by solving the linear balance equation, while the unbalanced part is analysed univariately (Derber and Bouttier, 1999). As the linear balance equation explains little variance of the wind field in the Tropics, the 3DVar analyses were effectively univariate in the Tropics. However, it is very different in 4DVar schemes; not only does the mass–wind adjustment within 4DVar extract information about the wind field from temperature data (Ruston and Healy, 2021), but the moisture observations also impact tropical winds significantly through 4DVar dynamics (Hólm *et al.*, 2002; Köpken *et al.*, 2004). There is, however, a limit to the wind information that can be extracted by 4DVar, even in the perfect-model case, which has been explained with the help of models of reduced complexity (Žagar *et al.*, 2004; Zaplotnik *et al.*, 2018).

In contrast, ensemble data assimilation makes no assumption about coupling between the mass-field variables and winds; the covariances are flow-dependent as derived from the ensemble of short-range forecasts. In this way, the impact of observations such as HLOS winds is distributed according to the flow properties (Šavli *et al.*, 2018). Modern 4DVar schemes estimate background variances from the ensemble of forecasts (Bonavita *et al.*, 2016), though correlations at the start of the 4DVar window are climatological. Derived from global forecast statistics, static correlations are characterised by longer scales in the Tropics (Ingleby, 2001; Pereira and Berre, 2006) than those found in ensemble Kalman filter (EnKF) data assimilation (Lei *et al.*, 2015). In practise, the EnKF is commonly combined with variational methods in so-called hybrid data assimilation (Houtekamer and Zhang, 2016; Bannister, 2017). These two methods have been considered comparable in global NWP, and continued progress (e.g. Buehner and Shlyaeva, 2015) suggests that relying more on fully flow-dependent covariance in hybrid data assimilation can lead to larger forecast improvements (Caron and Buehner, 2022).

The present study applies the EnKF to address the question of the relative value of mass-field and wind-field observations in the Tropics using a perfect-model framework. Multivariate data assimilation is performed by the ensemble adjustment Kalman filter system (EAKF: (Anderson *et al.*, 2009) with a homogeneous observation network and a relatively large ensemble to study the correlation lengths for different variables in relation to the flow. The comparison of wind information and mass information for the initialization of prediction models has been carried out many times in the past. Routinely performed observing-system experiments (OSEs) with NWP models compare the values of existing measurements and simulate the effects of planned components of the Global Observing System (GOS). For example, OSEs by Horányi *et al.* (2015a); Horányi *et al.* (2015b) with the European Centre for Medium-Range Weather Forecasts (ECMWF) 4DVar system showed that wind observations are on average more valuable in the upper troposphere, lower stratosphere, and Tropics, whereas mass data are more valuable in the lower troposphere of the midlatitudes in particular. This indicates that the information content of observations evolves with the GOS, forecast model, and data assimilation system.

Our perfect-model framework explores the upper limits on the information content of assimilated observations using observing-system simulation experiments (OSSEs). Such OSSEs were performed by Anderson *et al.* (2005) using the EnKF with an adiabatic model. They showed that the frequent assimilation of wind observations at the lowest model level produced analyses with errors only half as large as those from the assimilation of temperature data at the same level. In the present study, we employ a state-of-the-science moist model with the nature run forced by the observed sea-surface temperature. Effects of assimilated profiles of wind and temperature observations are compared with respect to flow-dependent

covariances. Given the properties of observations and the assimilation setup, this study provides an upper bound on the information content of winds and temperature fields that can be extracted from temperature and wind observations, respectively. We further compare the effects of temperature and wind observations on specific humidity, which is not an observed variable in our OSSEs.

The article is organised as follows. Section 2 describes the setup of the OSSEs, including the model, nature run, observation network, and data assimilation methodology. Section 3 presents the results, focusing on the average properties of the background and analysis ensembles for experiments assimilating only temperature, only winds, and both temperature and wind data. The multivariate aspects of assimilating different data types are discussed for the specific humidity variable. Differences among experiments are discussed using typical auto- and cross-correlations. A discussion, conclusions, and outlook are given in Section 4.

2 | PERFECT-MODEL ASSIMILATION EXPERIMENTS

The data assimilation framework is the ensemble adjustment Kalman filter system in the Data Assimilation Research Testbed (DART) (Anderson *et al.*, 2009), which is applied with the global Community Atmosphere Model (CAM, version 6.0.34) of the Community Earth System Model (CESM, version 2.1: Danabasoglu *et al.* (2020)). The perfect-model framework means that a single integration of the atmospheric component of CESM is taken to be the true state of the system. This is referred to as the "nature run" and used to create synthetic observations as described below. The preparation of OSSEs as described below and their evaluation is similar to that of Žagar *et al.* (2016), who used an earlier version of the CESM and did not consider temperature and wind observations separately. This task is carried out here using a more dense observation network and studying the effects of different observation types on the moisture field.

2.1 | Atmospheric model and nature run

We use the CAM6 model, an atmospheric component of CESM which uses the finite-volume (FV) dynamical core at a roughly 1 degree horizontal resolution. The model vertical discretisation is based on the hybrid sigma-pressure vertical coordinate, with 32 model levels including five levels below 900 hPa, nine levels above 100 hPa, and the top model level located at about 3.6 hPa. The FV dynamical core applies fourth-order divergence damping to the top three levels, increasing with height. The time step for coupling the physics to the dynamics is 30 min. There is no "time-splitting" in the dynamical core. Specific choices of the so-called CAM6 physics package are described in Raeder *et al.* (2021). The model is coupled to the land surface model known as the Community Land Model (CLM: Danabasoglu *et al.* (2020)). The sea-surface temperatures (SSTs) are prescribed and are derived from daily, 0.25 degree horizontal resolution, Advanced Very High Resolution Radiometer (AVHRR) data available from the National Centers for Environmental Information (the dataset was accessed on 2020-04-05 at http://dx.doi.org/10.5067/GHAAO-4BC02).

The initial atmospheric state for the nature run is taken from one member of the CAM6+DART Reanalysis project (Raeder *et al.*, 2021). This state is produced by the same model and the actual observations available at that time. We selected a winter period early in 2018 when one of the strongest Madden–Julian Oscillation (MJO) events on record took place (Barrett, 2019; Li *et al.*, 2020). While we do not expect our simulation to simulate the life cycle of the MJO realistically, the use of realistic SSTs leads to a more realistic representation of convection. The simulation starts on December 25, 2017 and runs until January 31, 2018.

2.2 | Synthetic observations

Synthetic observations are created as wind and temperature profiles from the nature run at 6-hr intervals. Observation errors typical of radiosondes are added to the profiles extracted from the nature-run simulation. The errors are randomly drawn from a Gaussian distribution having zero mean and standard deviation equal to the observation error taken from the Global Forecast System (GFS) observation-error tables from NCEP (valid in 2005) for the appropriate variable. The wind observation-error standard deviations increase from 1.4 $m \cdot s^{-1}$ at 1000 hPa up to 3.2 $m \cdot s^{-1}$ at 250 hPa and then decrease towards 2.1 $m \cdot s^{-1}$ at 40 hPa. The temperature-error standard deviations have values of 1.2 K at 1000, 250, and 200 hPa levels, and smaller values (0.8, 0.9, and 1.0 K) at other levels.

The idealized observation network is horizontally nearly homogeneous on the sphere (Figure 2). The network consists of 3456 grid points with an average horizontal separation of about 400 km. This is considered sufficient for the representation of large-scale features of the global atmosphere. A static, homogeneous observation network ensures that the flow-dependent covariances are not influenced by the distribution of observations (although they are influenced by the observation density). Profiles of the zonal and meridional winds and

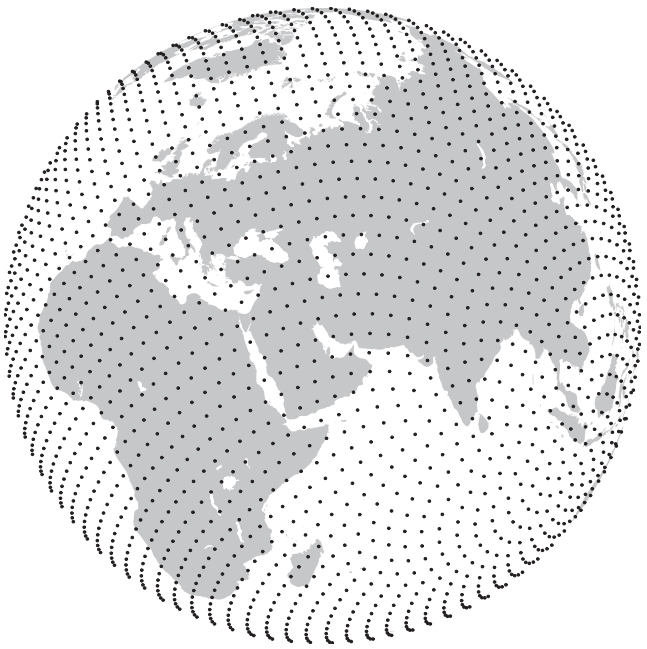

FIGURE 2 Homogeneous observation network for the observing-system simulation experiments. The network consists of 3456 locations of observations. At every location, vertical profiles of the temperature, zonal wind, and meridional wind are prepared from the nature run every 6 hr.

temperature are taken at the 21 mandatory pressure levels, with the exception of the 30-hPa level being replaced by 40 hPa to accommodate damping at the model top levels. In our perfect-model assimilation experiments, virtually all of the observations are assimilated, and the biases are very close to zero.

2.3 | Setup of the ensemble data assimilation

The data assimilation system DART applies the serial EAKF (Anderson, 2003; Anderson, 2009). The EAKF does not perturb observations. Analysis increments are calculated by shifting the prior mean and reducing its standard deviation using the normally distributed observation likelihood. Corresponding increments are computed for each ensemble member. The implementation of the EAKF includes vertical and horizontal covariance localisation using the function derived by Gaspari and Cohn (1999) to filter noisy background-error covariances by limiting the length of spatial correlations. The half-width radius for the horizontal localisation is 0.15 rad (around 955 km) and that for vertical localisation is 0.225 scale heights, which is 125 hPa near 500 hPa, but only 12.5 hPa near 50 hPa. The model state vector consists of temperature, meridional and zonal winds, specific humidity, cloud liquid and ice, and surface pressure. The observation operators interpolate the model values to the locations of observations linearly in the horizontal and linearly in log (pressure) in the vertical. All model state variables can be changed by the assimilation, but there are no observations above 40 hPa, so vertical localization of the observations means that the influence of the observations weakens with height in the top five model levels. The enhanced adaptive inflation of El Gharamti (2018) is used to maintain the ensemble spread at the levels needed for effective assimilation cycling. The inflation is spatially and temporally varying and applied to the prior ensemble. The inflation standard deviation, which controls how fast the inflation adapts, is fixed at 0.6. An inflation damping value of 0.9 is used, so that the inflation strength is reduced to 90% of its present value before being updated at each assimilation time. Both of these are the default values and are discussed in more detail in El Gharamti (2018). The assimilation also employs sampling-error correction (Anderson, 2012), which applies a heuristic correction to the ensemble spread to help overcome deficiencies due to limited ensemble size.

The initial, 80-member ensemble valid at 0000 UTC on December 25, 2017 is taken from the CAM6+DART Reanalysis (Raeder *et al.*, 2021). Observations are assimilated every six hours. During the first week of the experiment, the ensemble adjusts to the assimilated synthetic observations. Three assimilation experiments are carried out:

1. only temperature observations (experiment denoted *T*),
2. observations of both wind components (experiment denoted *UV*), and
3. both temperature and wind observations (experiment denoted *TUV*).

With respect to *Aeolus*, the experiment *UV* contains twice as many observations, since *Aeolus* measures a single wind component, the projection of the wind vector on the horizontal line of sight, the so-called HLOS winds. This is a special feature of the *Aeolus* Doppler wind lidar (Reitebuch, 2012), as wind measurements are usually observations of both wind components. The fact that the *UV* experiment assimilates twice as many observations as the *T* experiment is thus natural.

2.4 | Metrics

We used several metrics to measure the data assimilation performance and the impact of assimilating various observations, including the root-mean-square error (RMSE) of the ensemble mean compared with the nature run and the

square root of the ensemble variance, referred to as the ensemble spread. The RMSE can be written as

$$RMSE = \sqrt{< (x_t - \bar{x})^2 >}, \quad (3)$$

where <> denotes the spatial or temporal averaging (or both) of the squared errors, $\bar{x}$, is the ensemble mean and x_t stands for the true state of the variable x. The "averaged spread" for variable x is denoted σ_x and is the square root of the averaged ensemble variance V: $\sigma_x = \sqrt{< V_x >}$, where the unbiased ensemble variance at a single time step is

$$V_x = \frac{1}{N-1}\sum_{n=1}^{N}\left(x_n - \bar{x}\right)^2 \quad (4)$$

and $N = 80$ is the ensemble size.

The information content of observations is measured by the fractional reduction of the prior (6-hr forecast) ensemble spread by the assimilation of observations. The reduction can be calculated as the difference between the prior (or forecast) and *posterior* (or analysis) ensemble spread divided by the prior ensemble spread, that is, $1 - \sigma_x^{po}/\sigma_x^{pr}$, where "pr" and "po" denote the prior and posterior ensemble, respectively. In the rest of this article, we shall be using the expressions forecast (or background) ensemble and analysis ensemble, which are commonly used in the NWP community (rather than prior and posterior, typically used in the EnKF literature).

The correlations are calculated from the ensemble, selecting points in regions with strong precipitation and in areas without precipitation with a relatively low relative (and specific) humidity. For a variable x at the point (λ, φ, η), the correlation with variable y at the surrounding points $(\lambda', \varphi', \eta')$, r_{xy} is computed from the ensemble using the following formula:

$$r_{xy} = \frac{(N-1)^{-1}\sum_{n=1}^{N}\Delta x_n(\lambda,\varphi,\eta)\ \ \Delta y_n(\lambda',\varphi',\eta')}{\sqrt{V_x(\lambda,\varphi,\eta)\ \ V_y(\lambda',\varphi',\eta')}}, \quad (5)$$

where $\Delta x_n = x_n - \bar{x}$ is a deviation from the ensemble mean for the nth ensemble member. Indices λ, φ, η represent the longitude, latitude, and hybrid vertical model level, respectively. For autocorrelations, $x = y$, otherwise $x \neq y$ represents cross-correlations.

3 | COMPARISON OF THE EFFECTS OF TEMPERATURE AND WIND OBSERVATIONS

We start the discussion of the results by showing that our experiments are reliable. Then we present time- and space-averaged ensemble spread for the three experiments, demonstrating their similarities and differences. Focusing on the Tropics, we present case studies that illuminate coupling between the temperature, wind, and moisture observations in the EnKF.

3.1 | Evolution of the ensemble spread and ensemble reliability

The evolution of the vertically and horizontally averaged ensemble spread in analyses and 6-hr forecasts is shown in Figure 3. In each panel, the ensemble spread is averaged vertically up to 100 hPa and horizontally for different regions: the Tropics defined between 20°S and 20°N, and the extratropical Northern Hemisphere and Southern Hemisphere (NH and SH, respectively) up to 70°. On average, the experiments take about 2 weeks to reach a stable state, except for the extratropical temperature variable in the *UV* experiment, which is still equilibrating in the last two weeks of the experiment. The slow equilibration is limited to the lower stratosphere in high latitudes, particularly the SH, but the reasons are not fully understood.

The spread for the wind variables is smaller for the *UV* than for the *T* experiment, as expected. Adding temperature data on top of the wind observations (*TUV* experiment) leads to a further small reduction of the spread in every region (Figure 3, panels a1–b4). The spread absolute difference $T - TUV$ is greater than $UV - TUV$ everywhere, and much more so in the Tropics. There is no significant difference in the results for the two wind components. Somewhat different results can be seen in the evolution of temperature spread in the three experiments (Figure 3, c1–c4). In this case, wind observations (*UV* experiment) lead to a smaller spread in the temperature field not only in the Tropics but also in the extratropics after the first 2 weeks of the experiments. The spread absolute difference $T - TUV$ is over three times greater than $UV - TUV$. Adding temperature data on top of wind observations reduces extratropical temperature spread further. Overall, Figure 3 suggests that wind observations constrain the temperature field better than temperature data, in agreement with the classical argument presented in Figure 1.

The effect of wind and temperature observations on the specific humidity, a variable affected by the assimilated observations only indirectly, also differs in the Tropics and extratropics (Figure 3, d1–d4). The spread is greater in the Tropics than in the extratropics in all three experiments, since the specific humidity is largest in the Tropics. The difference between the spread in the *T* and *UV* experiments is also greater in the Tropics than outside them, suggesting a relatively stronger effect of winds on moisture

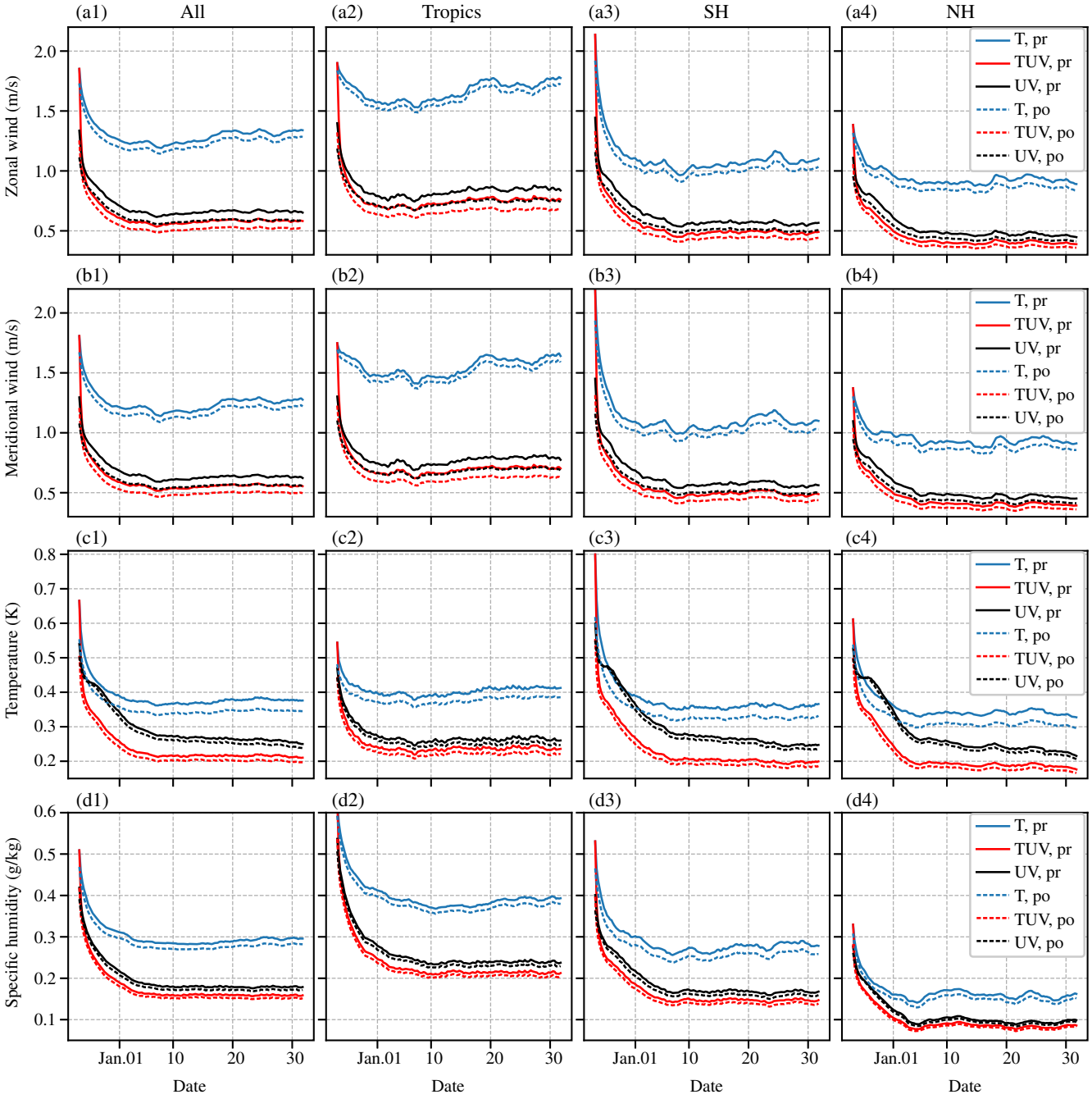

FIGURE 3 Time evolution of the ensemble spread in six-hour forecasts and analyses. (a1–d1) All points, (a2–d2) Tropics, (a3–d3) Southern Hemisphere (SH), and (a4–d4) Northern Hemisphere (NH) for (a1–a4) zonal wind, (b1–b4) meridional wind, (c1–c4) temperature, and (d1–d4) specific humidity in the three experiments. Different curves and experiments are explained in the legends: only temperature observations (*T*), only wind observations (*UV*), and both temperature and wind data (*TUV*). Analysis and forecast ensembles are denoted as po and pr and shown by dashed and full lines, respectively. Hemispheric results are averaged between 20° and 70°, Tropics are defined as the belt 20°S–20°N, and global results are between 70°S and 70°N. Vertically, results are averaged for all levels up to 100 hPa. [Colour figure can be viewed at wileyonlinelibrary.com]

closer to the Equator. As specific humidity is more directly related to temperature than to winds, the better analysis and forecast of the temperature field in the *UV* experiments lead to a more accurate moisture field. In addition, more accurate winds advecting the moisture, wherever advection takes place, improve the moisture field more in the experiments assimilating the winds.

Based on Figure 3, we compute statistics for the last three weeks of the experiments, January 11–31, 2018, at model levels. The time-average ensemble spread is

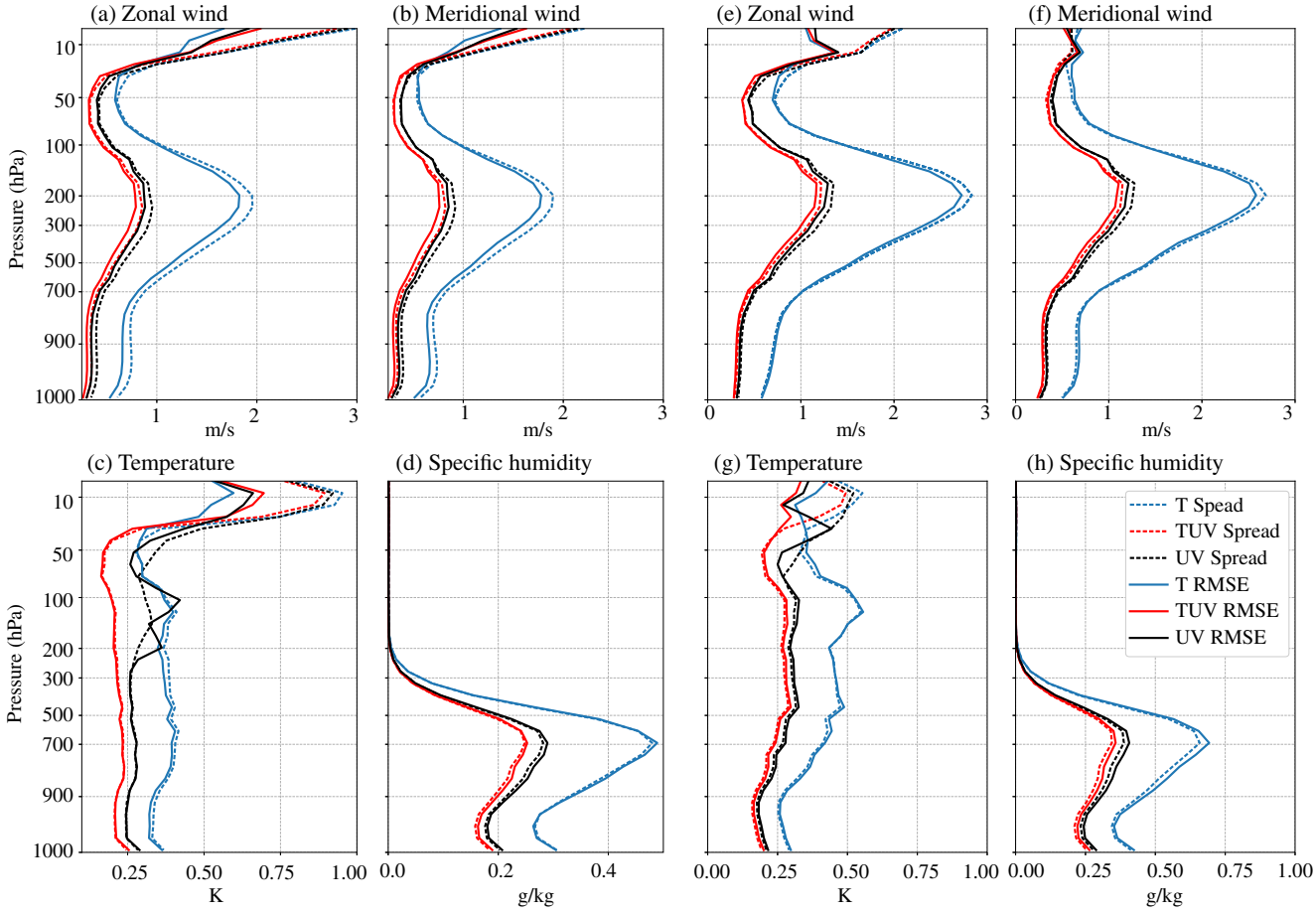

FIGURE 4 Reliability of OSSEs: (a–d) global and (e–h) tropical ensemble spread (dashed lines) in comparison with the root-mean-square error (RMSE, solid lines) for the three experiments and four variables in the 6-hr forecast ensemble. The results are averaged over the last three weeks of January 2018. [Colour figure can be viewed at wileyonlinelibrary.com]

compared with the RMSE in Figure 4 to display the reliability of the experiments. Reliability refers to the statistical consistency of the predicted probabilities as measured by the ensemble spread and the RMSE (Leutbecher and Palmer, 2008). The agreement between the two measures shows that the assimilation maintains a close agreement with the noisy observations. The comparison is shown separately for the Tropics and global atmosphere, to highlight the reliability of the tropical results in all experiments and variables. Reliability of the analysis ensemble is better than that of the forecast ensemble; the mean absolute differences between the spread and RMSE for the wind components are 24%–27% smaller for the analysis than for the forecast ensemble (not shown). An exception is the *UV* experiment, which is unreliable for the mass field above 200 hPa, due to issues at high latitudes (Figure 4c). Except for this, the RMSE is on average close to the spread up to about 30 hPa, as no observations were assimilated above this level. As we focus on the troposphere, subsequent discussion of the results will ignore the levels above 30 hPa and latitudes north and south of 70°. All subsequent figures will apply averaging over the last three weeks of the experiments, January 11–31, 2018.

3.2 | Latitude- and altitude-dependent properties of the ensemble

Having established the reliability of our experiments, we now compare results of the three experiments as a function of latitude. It is evident in Figure 5 that the largest uncertainties in global short-range forecasts are in the UTLS region in all three experiments. The maximal spread is near the 200-hPa level just slightly south of the Equator, related to the location of the Intertropical Convergence Zone (ITCZ) in January. This figure corroborates the earlier results by Žagar *et al.* (2016) from a *TUV* experiment without inflation and with a less dense observation network, as well as the properties of operational NWP ensembles such as the ECMWF. New results allow a comparison

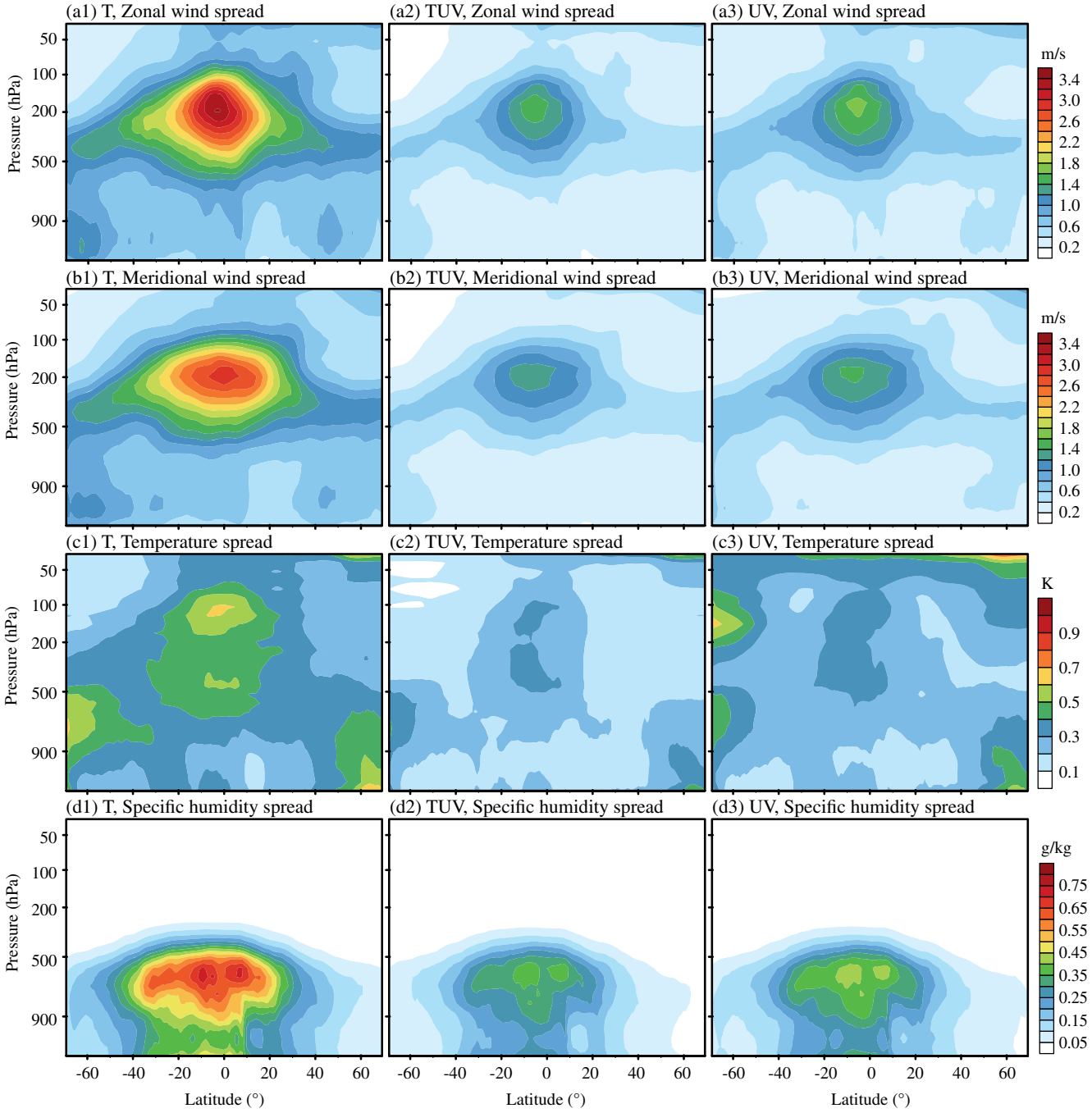

FIGURE 5 Zonally averaged spread of 6-hr forecast ensemble in (a1–a3) zonal wind, (b1–b3) meridional wind, (c1–c3) temperature, and (d1–d3) specific humidity in *T*, *UV*, and *TUV* experiments. Results are averaged over the last three weeks of January 2018. [Colour figure can be viewed at wileyonlinelibrary.com]

between experiments assimilating wind and temperature observations and their impact on specific humidity, as discussed next.

The ensemble spread for the wind components within the UTLS in the *UV* experiment is less than half that in the *T* experiment, and reduces further by a small factor in the *TUV* experiment. For instance, the zonal wind spread in the UTLS has a maximum of 1.51 $m \cdot s^{-1}$ in TUV, 1.68 $m \cdot s^{-1}$ in the *UV* experiment, and 3.4 $m \cdot s^{-1}$ in the *T* experiment (Figure 5, panels a1–a3). The effects of different observations on the temperature field are displayed in panels c1–c3. They show a smaller spread in the temperature field in the *UV* experiment than in the *T* experiment. This not only confirms the dynamical arguments displayed in Figure 1 in the global NWP context, it also suggests that a system with an abundance of wind observations makes

the temperature data in the Tropics and subtropics largely uninformative.

The latitude–altitude structure of the specific humidity spread, not studied by Žagar *et al.* (2016), shows a large spread in the tropical lower troposphere, where the largest moisture content also exists (Figure 5, panels d1–d3). The spread in the three experiments has similar structure, but amplitudes are twice as great in the *T* experiment as in experiments that assimilated winds. Large vertical gradients are present in the middle troposphere above the spread maxima near 600 hPa and across subtropical latitudes. In the next section, we look into the longitudinal structure of the moisture spread in relation to the flow.

3.3 | Flow-dependent effects of the assimilation of temperature and wind observations in the Tropics

Our perfect-model ensemble filter provides flow-dependent background errors without effects of the inhomogeneous observation network of the real world. While it seems evident that dynamical arguments derived from quasigeostrophic theory for adiabatic, barotropic motions apply in the moist, stratified atmosphere, we have limited understanding of factors shaping the altitude–longitude variations in the spread. This section aims to explain differences between the assimilation of temperature and wind observations.

The longitudinal behavior in the Tropics is presented in Figure 6 in the form of Hovmöller diagrams. First we notice similar spatial patterns in the spread for zonal wind and temperature at the level of the maximal zonal wind spread near 122 hPa (panels a1–d3). Analysis uncertainties are shown, but the patterns in the 6-hr forecast ensemble differ only in amplitude. We also always show ensemble spread, but the RMSE patterns have a very similar structure. The largest uncertainties for both zonal wind and temperature are over the Indian Ocean near the edge of the strong easterlies between 60°E and 90°E (Figure 6a–c). The secondary spread maxima in the *T* experiment are over the eastern Pacific, in the region with significant longitudinal gradient in the westerlies. This was an active period of MJO with phases 2 and 3 over the Indian Ocean during January 1–16, and an intensification during January 25–31, as the MJO was moving from the Maritime Continent to the Western Pacific in phases 5 and 6 (Barrett, 2019; Li *et al.*, 2020). Although we have not specifically investigated whether our nature run reproduced the MJO signal as measured by standard MJO indices, the increasing eastward-propagating coherent structure of the zonal wind spread during the last week of January (Figure 6 panels a1–3) could be associated with the MJO, similar to the case reported by Žagar *et al.* (2013) for the operational ECMWF ensemble.

The three experiments show very similar patterns of temporal spread evolution, although the amplitudes vary. The differences between experiments *TUV* and *UV* are hardly noticeable, in both the spread (Figure 6a,b) and the ensemble mean (Figure 6c). The latter is confirmed by the difference between the ensemble means among various experiments in Figure 6d. They show coherent structures moving eastward and westward in the regions of easterlies and westerlies, respectively. The difference between experiments with and without assimilation of wind observations can be as large as $\pm 10\ \mathrm{m \cdot s^{-1}}$ (Figure 6, panels d2, d3), while adding temperature observations on top of wind data produced an order-of-magnitude smaller change in the analyses (Figure 6, panel d1). We speculate that the differences correspond to those convective systems that require wind observations for their initialisation. This is supported by the specific humidity spread presented for the level near 524 hPa in Figure 6e. Increased specific humidity spread appears in the *T* experiment every few days near 150°E, which corresponds roughly to the originating points of the coherent structures in the wind spread. The same region is characterised by large longitudinal moisture gradients in the ensemble mean specific humidity (Figure 6f). Overall, moisture spread can be as large as 50% of the ensemble mean value of specific humidity in the *T* experiment near the edges of significant longitudinal gradients in the zonal winds.

The selected vertical level in Figure 6 is within the tropical tropopause layer (TTL), where the vertical shear of the zonal wind is largest. The vertical shear depends on the phase of the Quasi-Biennial Oscillation (QBO), which in turn was shown to affect the short-range forecast errors (Žagar *et al.*, 2007). In January 2018, the westerly QBO phase was transitioning to the easterly phase and the shear in the lower stratosphere was relatively weak. However, near the 100-hPa level the shear was significant, as illustrated in Figure 7 for January 11 and 31, showing the zonal wind spread superimposed on the ensemble mean zonal wind. Here we show only *T* and *UV* experiments, since the *TUV* experiment is almost indistinguishable from the *UV* experiment by visual inspection. Figure 7 shows the analysis ensemble, and the difference for the background ensemble is only in the magnitudes of the spread. Thus, Figure 7, together with Figure 6, illuminates the fact that the largest analysis and short-term forecast uncertainties in the Tropics are in the regions with the strongest vertical and longitudinal shear of the zonal wind. An accurate representation of this layer in the models is crucial for the vertically propagating equatorial waves driving the middle atmosphere circulation.

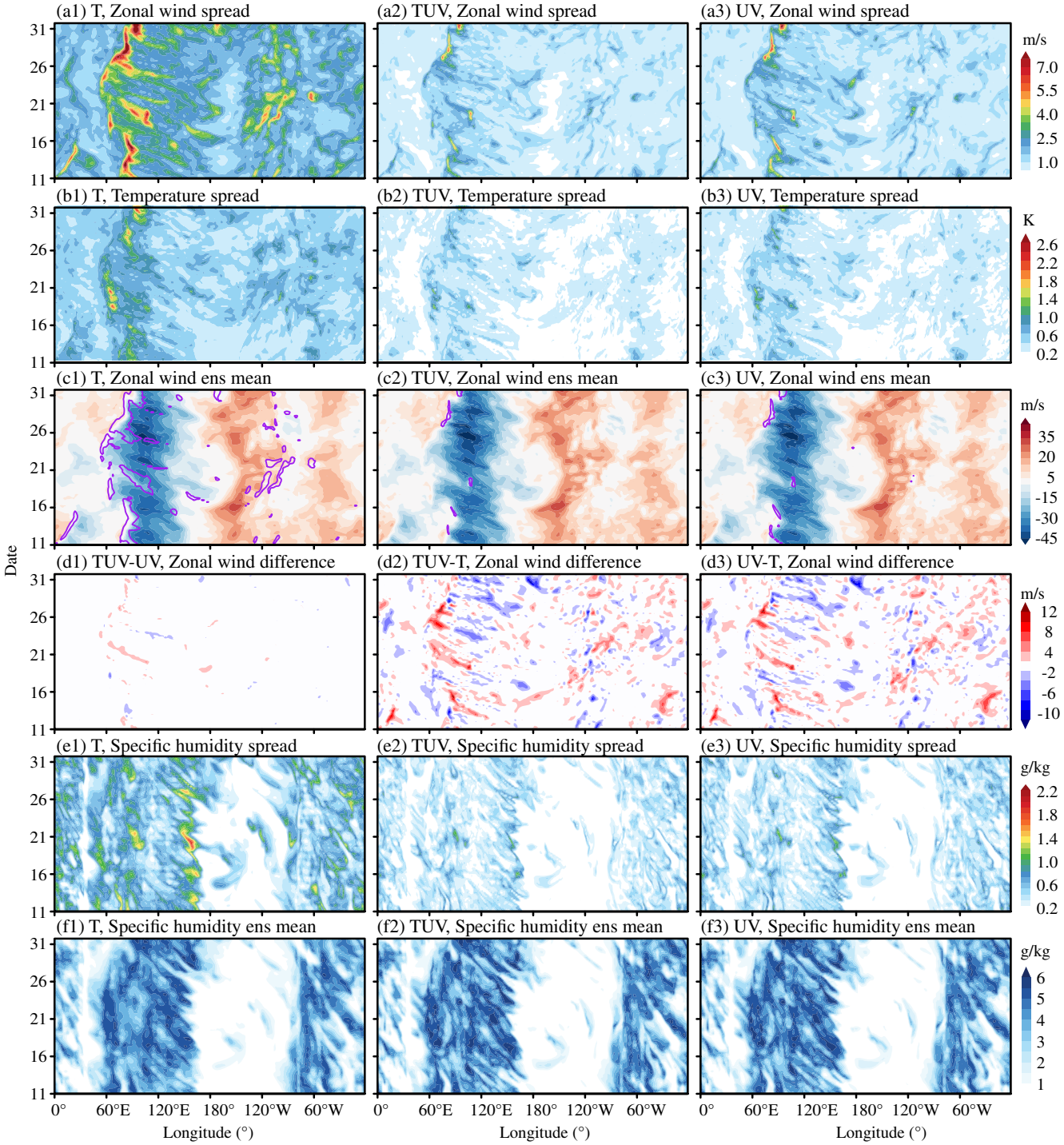

FIGURE 6 Evolution of the analysis ensemble mean zonal wind and specific humidity and evolution of the analysis ensemble spread of the zonal wind, temperature, and specific humidity along the latitude 0.5°N at the 122-hPa level (level 524 hPa for the specific humidity) during January 11–31, 2018. (a1–a3) Zonal wind spread, (b1–b3) temperature spread, (c1–c3) ensemble mean zonal wind, and (d1–d3) differences between the ensemble means of (d1) *TUV* and *UV*, (d2) *TUV* and *T*, and (d3) *UV* and *T* experiments. Specific humidity (e1–e3) spread and (f1–f3) ensemble mean. Magenta contours in (c1–c3) denote zonal wind spread greater than 4 $m \cdot s^{-1}$. [Colour figure can be viewed at wileyonlinelibrary.com]

Within the TTL, maximal temperature spread does not appear collocated with the maximal spread in the zonal wind, suggesting a nontrivial coupling between the two variables. The meridional wind spread has amplitudes as large as the zonal wind spread; it ranges between 1 and 5 $m \cdot s^{-1}$ in the layer between 500 and 100 hPa in the *T* experiment, whereas it nowhere exceeds 1.5 $m \cdot s^{-1}$ in the *UV* and *TUV* experiments (not shown). It must be

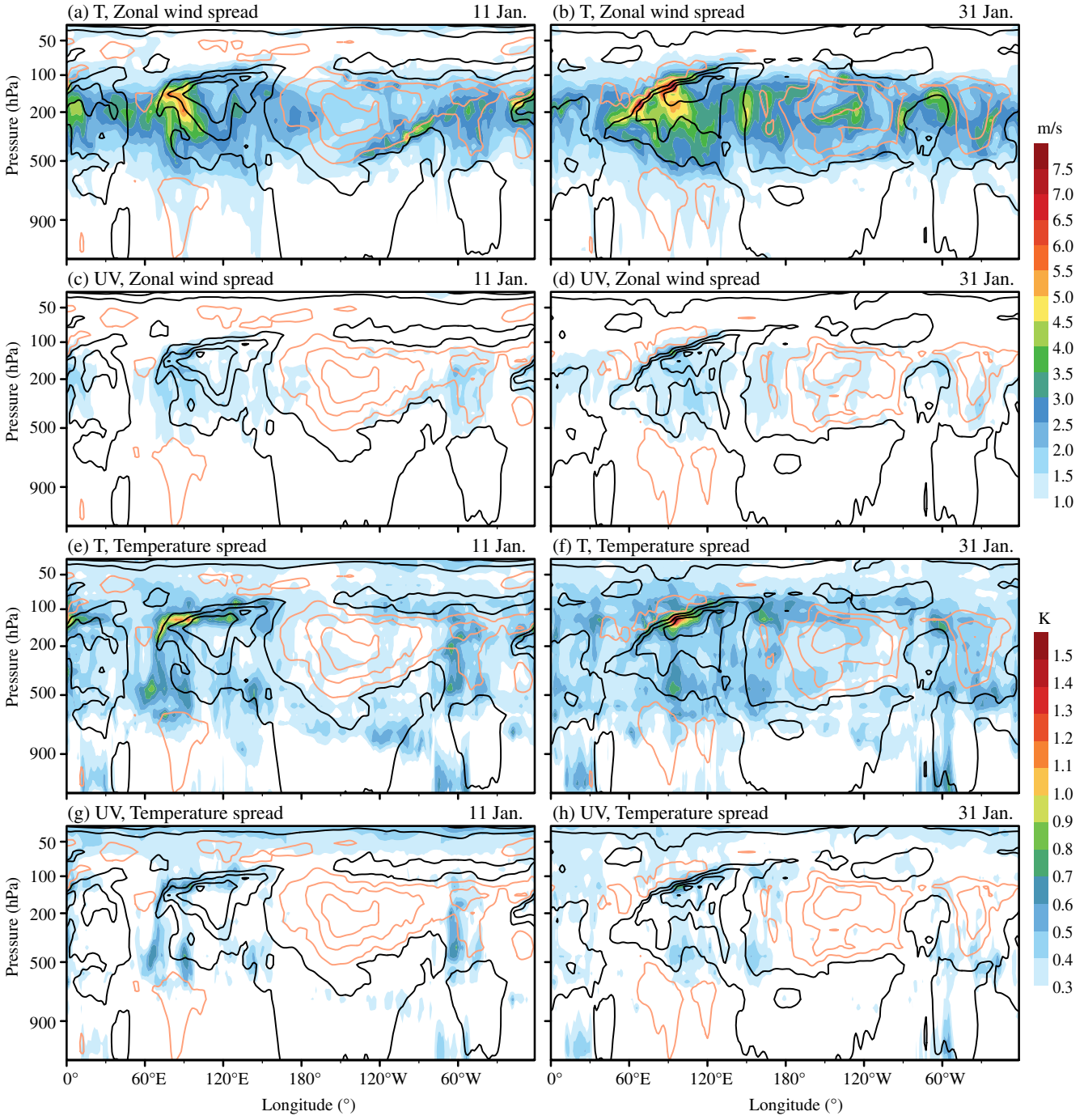

FIGURE 7 Vertical cross-section along the Equator of the analysis ensemble mean zonal wind (contours) and the zonal wind and temperature uncertainty (analysis ensemble spread, shading) for (a,b,e,f) *T* and (c,d,g,h) *UV* experiments on (left) January 11 and (right) January 31. The dark and light lines denote easterlies and westerlies, respectively, with contours every 10 $m \cdot s^{-1}$ starting at ± 5 $m \cdot s^{-1}$, and the zero isoline omitted. Results are averaged for 10 latitudes between 5°S and 5°N. [Colour figure can be viewed at wileyonlinelibrary.com]

mentioned that, in contrast to the zonal wind, the meridional wind is less than 10 $m \cdot s^{-1}$ everywhere except in the Amazon region. For the two dates shown in Figure 7, the spread is 2–3 times greater in the *T* than in the *UV* experiment, in agreement with Figures 4 and 5. The average reduction of the zonal wind background spread within the tropical UTLS in the two cases presented is at best 2%–5% in the *T* experiment, whereas it is up to 20% in the experiments with wind data (not shown). Here the background spread reduction means the difference between prior (or background) and posterior (or analysis) ensemble spread normalised by the spread of the forecast ensemble and multiplied by 100%, that is, $\left(1 - \sigma_x^{po}/\sigma_x^{pr}\right) * 100\%$ (Section 2). Similarly, the spread of 6-hr forecasts of

specific humidity is reduced by 1%–3% within the TTL in the *T* experiment compared with 5%–7% in the *UV* and *TUV* experiments (not shown). In contrast, the humidity spread reduction below 200 hPa is nearly the same in the three experiments, despite their differences in the spread (Figure 5j–l). This nonintuitive result is discussed next by investigating details of the coupling between winds and moisture and between the temperature and moisture variables.

3.4 | Tropical mass–wind covariances in the EAKF

Figure 8 presents the cross-correlations between the background errors in temperature and specific humidity for January 11 at two points, one in the precipitating region near 125°E and another in the nonprecipitating area of westerlies in the eastern Pacific near 120°W. It shows that the horizontal and vertical correlations have opposite signs in the saturated and unsaturated regions. The horizontal correlation length-scales are small, especially in the nonprecipitating region; correlations greater than ±0.2 are limited to 2, 3 and 5, 6 grid points for nonprecipitating and precipitating regions, respectively. With the grid spacing of 1°, the correlation length-scales are thus just a few 100 km. In the vertical, correlations in the precipitating region extend throughout the prescribed vertical localisation radius. In contrast, temperature-specific humidity correlations in the nonprecipitating region are limited to a single layer leaning towards the level above. The two chosen points are representative of similar locations we analysed at other dates and at other levels in the upper troposphere. Correlations of specific humidity with winds are weak and have small horizontal and vertical scales (not shown), though the horizontal correlations are stronger in the unsaturated regions, whereas the vertical correlations are deeper in precipitating regions, similar to temperature. Both temperature–wind and wind–temperature correlations are weak, in agreement with the weak mass–wind coupling in the Tropics (not shown).

How can we understand opposite signs of temperature-specific humidity error correlations in relation to the flow? In precipitating regions, the atmosphere is saturated and a positive increment in temperature is associated with an increase in saturation humidity via the Clausius–Clapeyron equation. There is sufficient moisture in the air to satisfy the saturation moisture required by the Clausius–Clapeyron relationship, meaning that the specific humidity is increased. The correlations are therefore positive both horizontally and vertically, as seen in Figure 8. In the areas without precipitation and with low specific humidity, such as near 120°W (see Figure 6f), negative correlations between temperature and specific humidity in the nearby points can be understood as being due to radiative cooling. A negative temperature perturbation in unsaturated flow is associated with a positive pressure perturbation at the same model level, meaning that the level will be found somewhat lower down in the troposphere, where the specific humidity is higher. Computations of ensemble perturbations in temperature and pressure confirm their opposite signs and weak temperature-specific humidity correlations nearly everywhere in the upper troposphere away from saturated regions (not shown). Depending on the depth of convection, negative correlations are also found in the layer above the tops of the convective clouds.

The autocorrelations between background errors in dynamical variables are shown in Figure 9 at the same points as in Figure 8. On average, both temperature and wind autocorrelations are approximately isotropic and have horizontal scales well within the applied covariance localisation radius, with half-width of 0.15 rad (955 km). The horizontal scales of the correlations for the wind variables in the precipitating region are about half those in the nonprecipitating region. The correlations are elongated vertically in precipitating regions, especially for the wind variables. Among the three variables, the shortest horizontal and vertical autocorrelations are found for the temperature field, especially in nonprecipitating regions. While temperature autocorrelations in various areas of the Tropics call for more detailed correlation statistics, our conclusion regarding shorter horizontal and longer vertical autocorrelation lengths in precipitating regions than in regions without precipitation is similar to the results for the extratropics by Montmerle (2012) and Lei *et al.* (2015).

Moving away from the Equator, horizontal scales increase and stretch in the direction of the mean wind, so that their longer scale can be approximately 955 km in the subtropics (not shown). Longer correlation lengths in the stratosphere compared with the troposphere are seen in both middle latitudes and the Tropics, as expected. We stress that the tropical length-scales in Figure 8 do not increase with height within the troposphere, especially not in the precipitating regions. This is different from the extratropical troposphere outside regions of mesoscale convection, and also different from some earlier studies that argued that forecast-error correlation length-scales are longer in the Tropics compared with the extratropics (Ingleby, 2001; Pereira and Berre, 2006), although length-scales estimated using ensemble methods were shorter than those estimated using the NMC method (Pereira and Berre, 2006). The increase of the horizontal

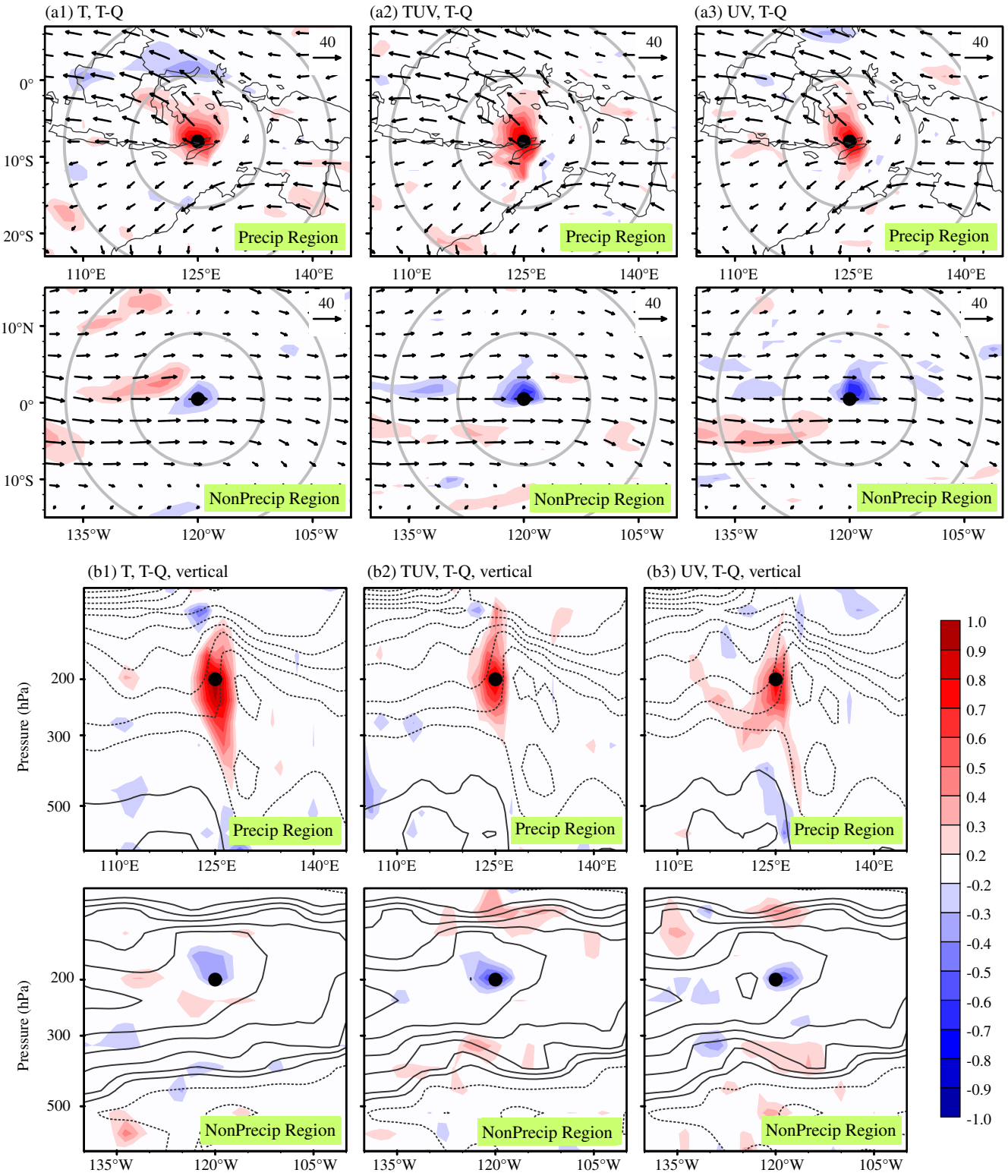

FIGURE 8 (a) Horizontal and (b) vertical cross-correlations between background errors in temperature and specific humidity in three experiments at model level 15 near 200 hPa at 0000 UTC on January 11, 2018. Two selected points represent precipitating areas (point 125°E, 8°S) and nonprecipitating regions (point 120°W, 0.5°N). The dashed and solid lines denote ensemble mean easterlies and westerlies, respectively, with contours every $\pm 5\ \mathrm{m \cdot s^{-1}}$ and the zero isoline omitted. The radii of the circles are 0.15 rad (955 km) and 0.3 rad, with 1 radian corresponding to 6371 km. The inner circle has a radius equal to the localisation radius. [Colour figure can be viewed at wileyonlinelibrary.com]

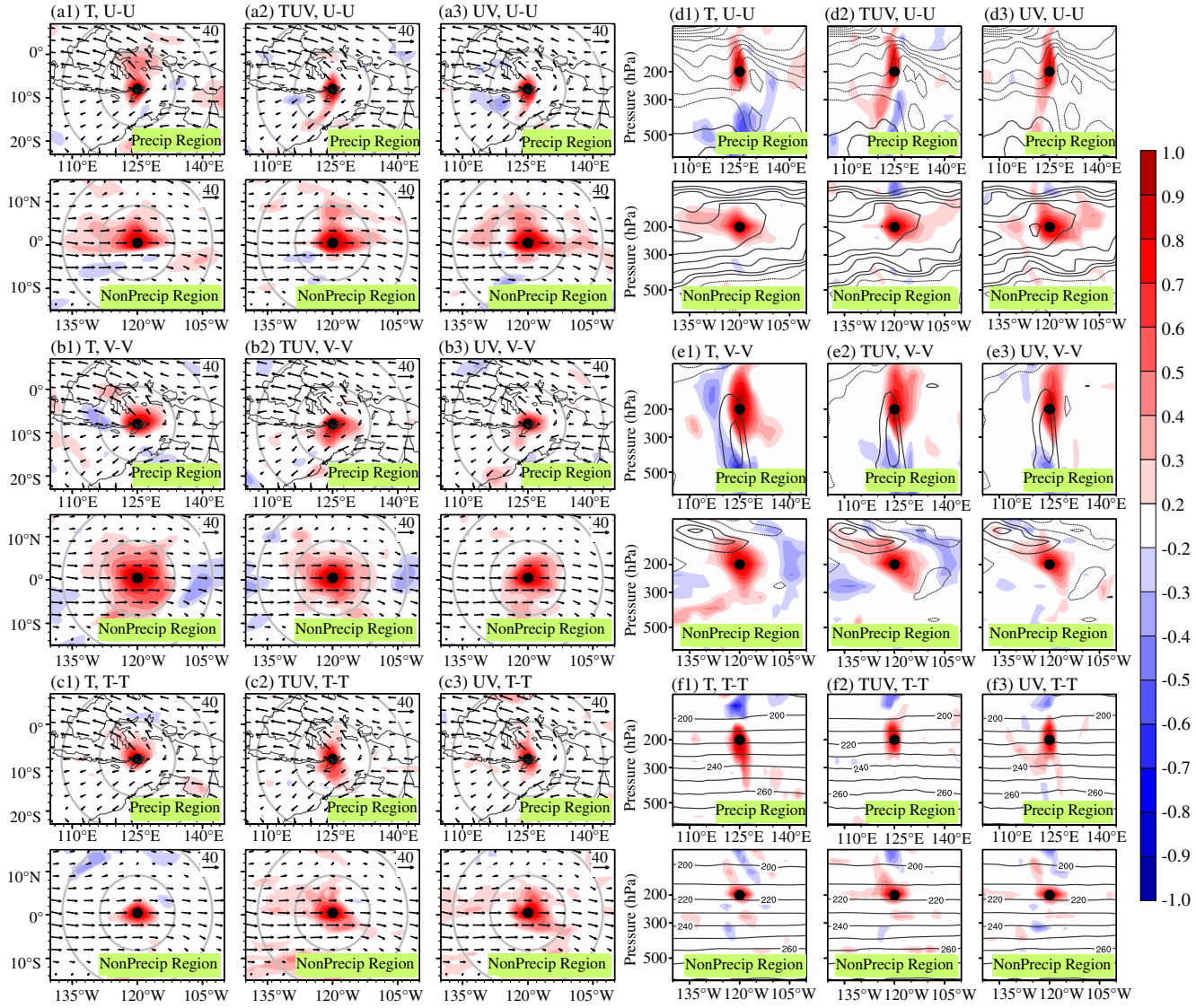

FIGURE 9 As in Figure 8, but (a–c) horizontal and (d–f) vertical autocorrelations. The ensemble mean (d) zonal wind and (e) meridional wind are shown every $\pm 5\ \mathrm{m \cdot s^{-1}}$, with solid lines for positive, dashed lines for negative, and the zero isoline omitted. The ensemble mean temperature in (f) is drawn every 10 K, starting from 190 K. [Colour figure can be viewed at wileyonlinelibrary.com]

correlation length-scale, when approaching the Equator, was argued to reflect the latitudinal dependence of the Rossby radius of deformation. In addition to different analysis methods, early studies often used 24-hr forecasts, a time-scale longer than the scale of the forecast-error growth due to convection.

Žagar *et al.* (2005) demonstrated that the short horizontal length-scales in the tropical troposphere are due to a combined effect of mass–wind couplings of equatorial waves. More recently, Lee and Huang (2020) have shown that shorter length-scales of the background errors are beneficial for convective-scale forecasting in the Tropics. Although we do not examine the global statistics of error correlation lengths, Figures 8 and 9 are examples relevant for all points we looked at. Figure 9 also shows that the smallest difference between the length-scales in precipitating and nonprecipitating regions is in temperature errors. This not only implies that moist convective processes affect the correlation scales for wind variables, but also suggests that temperature correlation scales in the Tropics may be influenced more by dynamics than by convection.

4 | SUMMARY AND OUTLOOK

In 1969, Smagorinsky discussed the problems and promises of deterministic extended range forecasting (Smagorinsky, 1969). It is worth citing his Orwellian tones about the relative importance of the wind and mass-field observations for deterministic forecasting: "Not all data

are equal in their information-yielding capacity. Some are more equal than others." He continued with, "This tells us that if there is a choice as to what can be measured, then one variable may be preferable over another. I'm sure this will turn out to be the case in the Tropics." Soon after, Gordon *et al.* (1972) demonstrated that the preferable variable is the wind. Moreover, Gordon *et al.* (1972) showed that the possible reduction of analysis uncertainties in the Tropics achieved by adding wind observations is expected to have a positive impact even on the forecast errors in the extratropics. Nevertheless, the GOS composed primarily of mass-field observations, that is, satellite observations of radiances, has been one of the key components of the great progress in NWP in the last two decades. Tens of millions of radiance observations are currently thinned and effectively filtered out in assimilation preprocessing (e.g. Liu and Rabier, 2002). With the successful launch of the *Aeolus* satellite and the assimilation of its HLOS wind profiles, the lengthy road towards closing the long-standing observation gap in the GOS has begun.

The percentage of wind observations in the GOS is less than 10% of the total number of observations that enter the operational data assimilation cycle at NWP centers (Horányi *et al.*, 2015a). However, the information content of wind observations is relatively greater than their number percentage, with the exact difference depending on the data assimilation system and NWP model (Baker *et al.*, 2014). The fact that *Aeolus* winds, in spite of their large random errors (in the Rayleigh channel), improve tropical analyses and forecasts in all operational NWP models is evidence of the limitations of mass-field observations, as discussed in the Introduction within a simple f-plane shallow-water framework. In fact, the *Aeolus* winds were also shown to correct systematic errors in the ECMWF model within the tropical tropopause layer (Rennie *et al.*, 2021; Bley *et al.*, 2022), improvements that may be crucial for the extratropical effects of better tropical analyses as argued by Gordon *et al.* (1972) half a century ago.

In operational NWP systems, inhomogeneous observation networks and statistically derived mass–wind correlations built into the background-error covariance model in variational data assimilation make it difficult to identify flow-dependent properties of analysis and forecast uncertainties. Our OSSEs with an EnKF and a perfect model provide a suitable framework for the computation of flow-dependent analysis and background errors for assimilated dynamical variables (temperature and wind components) and their multivariate coupling with the specific humidity, the balance properties of which are known to be complex (Bannister *et al.*, 2020). The auto- and cross-correlations are computed in precipitating and nonprecipitating regions in January 2018 and are used to discuss the spatial scales and strength of tropical mass–wind covariances. In reality, NWP models are not perfect and the observation network is inhomogeneous. Nevertheless, our results provide an understanding relevant for the current GOS and NWP and for planning future observing systems.

One of the key results of our study is that, in an ensemble Kalman filter data assimilation system with a perfect model and a wealth of wind observations, temperature observations provide little added value for tropical analyses. According to our results, wind data are more effective than temperature observations in constraining the tropical temperature field. The assimilation of only temperature data leads to systematic deficiencies in the background wind by missing propagating signals in the flow, especially in the easterlies east of the dateline. Furthermore, we have shown that the assimilation of wind observations is twice as effective as the assimilation of temperature observations in reducing the background specific moisture spread. Flow dependence of moisture background errors suggests that circulation (i.e., moisture convergence) is more important for the prediction of convection than local thermodynamics, as suggested by Hohenegger and Stevens (2013).

According to our results, all tropical error correlations are horizontally short. In particular, correlations of wind background errors have shorter horizontal and deeper vertical scales in precipitating regions compared with nonprecipitating areas. Tropospheric temperature correlations are much shorter than the applied localisation radius, suggesting that the horizontal localisation radii are not an issue in the ensemble data assimilation. Error correlations between temperature and specific humidity have small scales and opposite signs in precipitating (positive correlation) and nonprecipitating (negative correlation) regions, which can be explained by physical coupling between the two variables through the Clausius–Clapeyron equation and radiative cooling, respectively. The smallest difference between correlation length-scales in precipitating and nonprecipitating regions is found in temperature errors, suggesting that the temperature correlation scales in the Tropics may be influenced more by dynamics than by convection.

We do not make quantitative conclusions about the ratios between the background and analysis ensemble variances (or spread) in various experiments, as they depend on several choices in the OSSEs. The choice of observation-error variances is not considered problematic, as the short-range forecast skill in the Tropics seems insensitive to observation errors, in particular for the temperature field (Anderson *et al.*, 2005; Privé *et al.*, 2013; Privé *et al.*, 2021).

Flow-dependent structures of the analysis and forecast uncertainties (in terms of the ensemble spread) show that the uncertainties are largest in regions of strong vertical and longitudinal gradients in the background wind, irrespective of the dynamical variable and observation type. The largest spread is thus found in the UTLS region, especially over the Indian Ocean and Maritime Continent. The vertical wind shear has been shown to be underestimated in NWP models (Houchi *et al.*, 2010). Improving its representation is more feasible by using direct wind observations. That is consistent with our findings of large improvements in background winds at the edge of the easterlies in experiments that assimilated winds. In agreement with this finding, the *Aeolus* observations were shown to bring improvements in the vertically propagating equatorial Kelvin waves within the UTLS, leading to better forecasts in the tropical stratosphere (Žagar *et al.*, 2021).

With respect to the HLOS winds from *Aeolus*, our experiments make use of twice as many wind data, since both wind components are assimilated as typical for wind observing systems. Future Doppler wind lidars in space will hopefully employ technologies for measuring both wind components. While we have not compared the relative value of the two wind components, the OSEs with the ECMWF model by Horányi *et al.* (2015a) suggest that the zonal wind is more valuable, justifying the *Aeolus* HLOS winds being almost zonal. Additional experiments of the type applied here could quantify better the combined effects of moisture and temperature observations on the wind field in a perfect model, or the combined effect of temperature and HLOS winds for *Aeolus* follow-on missions.

Another remaining topic is the evaluation of mass and wind observations at high latitudes. It is worthwhile to note the limitation of mass-field information in polar regions, as discussed in the Introduction. Rennie *et al.* (2021) and other studies of the impact of *Aeolus* winds in NWP show significant positive impacts in the polar regions. Although the impact is likely influenced by the increasing number of *Aeolus* wind profiles in latitudes with otherwise little wind information (Sandu *et al.*, 2021), the relative value of mass- and wind-field data and examination of the cross-correlations between mass and wind variables in NWP models in polar regions remain to be investigated.

AUTHOR CONTRIBUTIONS

Lanqian Li: formal analysis; funding acquisition; investigation; validation; visualization; writing – original draft; writing – review and editing. **Nedjeljka Žagar:** conceptualization; formal analysis; funding acquisition; investigation; methodology; project administration; resources; supervision; validation; visualization; writing – original draft; writing – review and editing. **Kevin Raeder:** conceptualization; data curation; formal analysis; investigation; methodology; project administration; software; validation; writing – original draft; writing – review and editing. **Jeffrey L. Anderson:** conceptualization; data curation; funding acquisition; investigation; methodology; project administration; resources; software; supervision; writing – review and editing.

ACKNOWLEDGEMENTS

Lanqian Li gratefully acknowledges the financial support granted by the China Scholarship Council (CSC, grant no. 202106180040). Nedjeljka Žagar acknowledges the Deutsche Forschungsgemeinschaft (grant no. 461186383). The constructive comments of two anonymous reviewers are greatly appreciated. We also thank our colleagues Stefan Bühler and Cathy Hohenegger for discussion. The OSSE results were generated on NCAR's Cheyenne and Casper computer systems (NCAR CISL, 2019). NCAR is sponsored by the National Science Foundation. Any opinions, findings, and conclusions or recommendations expressed in this material do not necessarily reflect the views of the National Science Foundation. Open Access funding enabled and organized by Projekt DEAL.

CONFLICT OF INTEREST STATEMENT

We have no conflicts of interest to disclose.

ORCID

Lanqian Li https://orcid.org/0000-0001-7845-3702
Nedjeljka Žagar https://orcid.org/0000-0002-7256-5073

REFERENCES

Anderson, J., Hoar, T., Raeder, K., Liu, H., Collins, N., Torn, R. and Avellano, A. (2009) The data assimilation research testbed: a community facility. *Bulletin of the American Meteorological Society*, 90, 1283–1296.

Anderson, J.L. (2003) A local least squares framework for ensemble filtering. *Monthly Weather Review*, 131, 634–642.

Anderson, J.L. (2009) Spatially and temporally varying adaptive covariance inflation for ensemble filters. *Tellus A: Dynamic Meteorology and Oceanography*, 61 A, 72–83.

Anderson, J.L. (2012) Localization and sampling error correction in ensemble Kalman filter data assimilation. *Monthly Weather Review*, 140, 2359–2371.

Anderson, J.L., Wyman, B., Zhang, S. and Hoar, T. (2005) Assimilation of surface pressure observations using an ensemble filter in an idealized global atmospheric prediction system. *Journal of the Atmospheric Sciences*, 62, 2925–2938.

Baker, W.E., Atlas, R., Cardinali, C., Clement, A., Emmitt, G.D., Gentry, B.M., Hardesty, R.M., Källén, E., Kavaya, M.J., Langland, R.,

Ma, Z., Masutani, M., McCarty, W., Pierce, R.B., Pu, Z., Riishojgaard, L.P., Ryan, J., Tucker, S., Weissmann, M. and Yoe, J.G. (2014) Lidar-measured wind profiles: the missing link in the global observing system. *Bulletin of the American Meteorological Society*, 95, 543–564.

Bannister, R.N. (2017) A review of operational methods of variational and ensemble-variational data assimilation. *Quarterly Journal of the Royal Meteorological Society*, 143, 607–633.

Bannister, R.N., Chipilski, H.G. and Martinez-Alvarado, O. (2020) Techniques and challenges in the assimilation of atmospheric water observations for numerical weather prediction towards convective scales. *Quarterly Journal of the Royal Meteorological Society*, 146, 1–48.

Barrett, B.S. (2019) Connections between the madden–Julian oscillation and surface temperatures in winter 2018 over eastern North America. *Atmospheric Science Letters*, 20, e869.

Bley, S., Rennie, M., Žagar, N., Pinol Sole, M., Straume, A.G., Antifaev, J., Candido, S., Carver, R., Fehr, T., von Bismarck, J., Hünerbein, A. and Deneke, H. (2022) Validation of the Aeolus L2B Rayleigh winds and ECMWF short-range forecasts in the upper troposphere and lower stratosphere using loon super pressure balloon observations. *Quarterly Journal of the Royal Meteorological Society*, 148, 3852–3868.

Bonavita, M., Hólm, E., Isaksen, L. and Fisher, M. (2016) The evolution of the ECMWF hybrid data assimilation system. *Quarterly Journal of the Royal Meteorological Society*, 142, 287–303.

Buehner, M. and Shlyaeva, A. (2015) Scale-dependent background-error covariance localisation. *Tellus*, 67A, 28027.

Caron, J.-F. and Buehner, M. (2022) Implementation of scale-dependent background-error covariance localization in the Canadian global deterministic prediction system. *Weather and Forecasting*, 37, 1567–1580.

Daley, R. (1991) *Atmospheric Data Analysis*. Cambridge, UK: Cambridge University Press.

Danabasoglu, G., Lamarque, J.-F., Bacmeister, J., Bailey, D.A., DuVivier, A.K., Edwards, J., Emmons, L.K., Fasullo, J., Garcia, R., Gettelman, A., Hannay, C., Holland, M.M., Large, W.G., Lauritzen, P.H., Lawrence, D.M., Lenaerts, J.T.M., Lindsay, K., Lipscomb, W.H., Mills, M.J., Neale, R., Oleson, K.W., Otto-Bliesner, B., Phillips, A.S., Sacks, W., Tilmes, S., van Kampenhout, L., Vertenstein, M., Bertini, A., Dennis, J., Deser, C., Fischer, C., Fox-Kemper, B., Kay, J.E., Kinnison, D., Kushner, P.J., Larson, V.E., Long, M.C., Mickelson, S., Moore, J.K., Nienhouse, E., Polvani, L., Rasch, P.J. and Strand, W.G. (2020) The community earth system model version 2 (CESM2). *Journal of Advances in Modeling Earth Systems*, 12, e2019MS001916.

Derber, J. and Bouttier, F. (1999) A reformulation of the background error covariance in the ECMWF global data assimilation system. *Tellus A: Dynamic Meteorology and Oceanography*, 51, 195–221.

Derber, J.C. (1987) Variational four-dimensional analysis using quasi-geostrophic constraints. *Monthly Weather Review*, 115, 998–1008.

El Gharamti, M. (2018) Enhanced adaptive inflation algorithm for ensemble filters. *Monthly Weather Review*, 146, 623–640.

Emerton, R., Brimicombe, C., Magnusson, L., Roberts, C., Di Napoli, C., Cloke, H.L. and Pappenberger, F. (2022) Predicting the unprecedented: forecasting the June 2021 Pacific northwest heatwave. *Weather*, 77, 272–279.

Garrett, K., Liu, H., Ide, K., Hoffman, R.N. and Lukens, K.E. (2022) Optimization and impact assessment of Aeolus HLOS wind assimilation in NOAA's global forecast system. *Quarterly Journal of the Royal Meteorological Society*, 148, 2703–2716.

Gaspari, G. and Cohn, S.E. (1999) Construction of correlation functions in two and three dimensions. *Quarterly Journal of the Royal Meteorological Society*, 125, 723–757.

Gordon, C.T., Umscheid, L. and Miyakoda, K. (1972) Simulation experiments for determining wind data requirements in the tropics. *Journal of Atmospheric Sciences*, 29, 1064–1075.

Healy, S., Polichtchouk, I. and Horányi, A. (2020) Monthly and zonally averaged zonal wind information in the equatorial stratosphere provided by GNSS radio occultation. *Quarterly Journal of the Royal Meteorological Society*, 146, 3612–3621.

Hohenegger, C. and Stevens, B. (2013) Preconditioning deep convection with cumulus Congestus. *Journal of the Atmospheric Sciences*, 70, 448–464.

Hólm, E., Andersson, E., Beljaars, A., Lopez, P., Mahfouf, J.-F., Simmons, A. and Thépaut, J.-N. (2002) Assimilation and modelling of the hydrological cycle: ECMWF's status and plans. *ECMWF Technical Memoranda*, 383, 1–55.

Horányi, A., Cardinali, C., Rennie, M. and Isaksen, L. (2015a) The assimilation of horizontal line-of-sight wind information into the ECMWF data assimilation and forecasting system. Part I: the assessment of wind impact. *Quarterly Journal of the Royal Meteorological Society*, 141, 1223–1232.

Horányi, A., Cardinali, C., Rennie, M. and Isaksen, L. (2015b) The assimilation of horizontal line-of-sight wind information into the ECMWF data assimilation and forecasting system. Part II: the impact of degraded wind observations. *Quarterly Journal of the Royal Meteorological Society*, 141, 1233–1243.

Houchi, K., Stoffelen, A., Marseille, G.J. and De Kloe, J. (2010) Comparison of wind and wind shear climatologies derived from high-resolution radiosondes and the ECMWF model. *Journal of Geophysical Research: Atmospheres*, 115, D22123.

Houtekamer, P.L. and Zhang, F. (2016) Review of the ensemble Kalman filter for atmospheric data assimilation. *Monthly Weather Review*, 144, 4489–4532.

Ingleby, N.B. (2001) The statistical structure of forecast errors and its representation in the met. Office global 3-D Variational data assimilation scheme. *Quarterly Journal of the Royal Meteorological Society*, 127, 209–231.

Kalnay, E. (2003) *Atmospheric Modeling, Data Assimilation and Predictability*. Cambridge, UK: Cambridge University Press.

Kiladis, G., Wheeler, M., Haertel, P., Straub, K. and Roundy, P.E. (2009) Convectively coupled equatorial waves. *Reviews of Geophysics*, 47, RG2003.

Köpken, C., Kelly, G. and Thépaut, J.-N. (2004) Assimilation of Meteosat radiance data within the 4D-Var system at ECMWF: assimilation experiments and forecast impact. *Quarterly Journal of the Royal Meteorological Society*, 130, 2277–2292.

Laroche, S. and St-James, J. (2022) Impact of the Aeolus level-2B horizontal line-of-sight winds in the environment and climate change Canada global forecast system. *Quarterly Journal of the Royal Meteorological Society*, 148, 2047–2062.

Lee, J.C.K. and Huang, X.-Y. (2020) Background error statistics in the tropics: structures and impact in a convective-scale numerical weather prediction system. *Quarterly Journal of the Royal Meteorological Society*, 146, 2154–2173.

Lei, L., Anderson, J.L. and Romine, G.S. (2015) Empirical localization functions for ensemble Kalman filter data assimilation in regions with and without precipitation. *Monthly Weather Review*, 143, 3664–3679.

Leutbecher, M. and Palmer, T.N. (2008) Ensemble forecasting. *Journal of Computational Physics*, 227, 3515–3539.

Li, X., Mecikalski, J.R. and Lang, T.J. (2020) A study on assimilation of CYGNSS wind speed data for tropical convection during 2018 January MJO. *Remote Sensing*, 12, 1243.

Liu, Z.-Q. and Rabier, F. (2002) The interaction between model resolution, observation resolution and observation density in data assimilation: a one-dimensional study. *Quarterly Journal of the Royal Meteorological Society*, 128, 1367–1386.

Montmerle, T. (2012) Optimization of the assimilation of radar data at the convective scale using specific background error covariances in precipitation. *Monthly Weather Review*, 140, 3495–3506.

NCAR CISL. (2019) Cheyenne: HPE/SGI ICE XA System (NCAR Community Computing). doi:10.5065/D6RX99HX.

Pereira, M.B. and Berre, L. (2006) The use of an ensemble approach to study the background error covariances in a global NWP model. *Monthly Weather Review*, 134, 2466–2489.

Pourret, V., Šavli, M., Mahfouf, J.-F., Raspaud, D., Doerenbecher, A., Bénichou, H. and Payan, C. (2022) Operational assimilation of Aeolus winds in the Météo-France global NWP model ARPEGE. *Quarterly Journal of the Royal Meteorological Society*, 148, 2652–2671.

Privé, N., Errico, R. and Tai, K.-S. (2013) The influence of observation errors on analysis error and forecast skill investigated with an observing system simulation experiment. *Journal of Geophysical Research: Atmospheres*, 118, 5332–5346.

Privé, N.C., Errico, R.M. and McCarty, W. (2021) The importance of simulated errors in observing system simulation experiments. *Tellus A: Dynamic Meteorology and Oceanography*, 73, 1–17.

Raeder, K., Hoar, T.J., El Gharamti, M., Johnson, B.K., Collins, N., Anderson, J.L., Steward, J. and Coady, M. (2021) A new CAM6+ DART reanalysis with surface forcing from CAM6 to other CESM models. *Scientific Reports*, 11, 1–24.

Reitebuch, O. (2012) The spaceborne wind lidar mission ADM-Aeolus. In: Schumann, U. (Ed.) *Atmospheric Physics*. Berlin, Heidelberg: Research Topics in Aerospace. Springer, pp. 815–827.

Rennie, M.P., Isaksen, L., Weiler, F., de Kloe, J., Kanitz, T. and Reitebuch, O. (2021) The impact of Aeolus wind retrievals on ECMWF global weather forecasts. *Quarterly Journal of the Royal Meteorological Society*, 147, 3555–3586.

Ruston, B. and Healy, S. (2021) Forecast impact of FORMOSAT-7/COSMIC-2 GNSS radio occultation measurements. *Atmospheric Science Letters*, 22(22), e1019.

Sandu, I., Massonnet, F., van Achter, G., Acosta Navarro, J.C., Arduini, G., Bauer, P., Blockley, E., Bormann, N., Chevallier, M., Day, J., Dahoui, M., Fichefet, T., Flocco, D., Jung, T., Hawkins, E., Laroche, S., Lawrence, H., Kristiansen, J., Moreno-Chamarro, E., Ortega, P., Poan, E., Ponsoni, L. and Randriamampianina, R. (2021) The potential of numerical prediction systems to support the design of Arctic observing systems: insights from the APPLICATE and YOPP projects. *Quarterly Journal of the Royal Meteorological Society*, 147, 3863–3877.

Šavli, M., Žagar, N. and Anderson, J.L. (2018) Assimilation of horizontal line-of-sight winds with a mesoscale EnKF data assimilation system. *Quarterly Journal of the Royal Meteorological Society*, 144, 2133–2155.

Smagorinsky, J. (1969) Problems and promises of deterministic extended range forecasting. *Bulletin of the American Meteorological Society*, 50, 286–312.

Stoffelen, A., Pailleux, J., Källén, E., Vaughan, J.M., Isaksen, L., Flamant, P., Wergen, W., Andersson, E., Schyberg, H., Culoma, A., Meynart, R., Endemann, M. and Ingmann, P. (2005) The atmospheric dynamics mission for global wind field measurement. *Bulletin of the American Meteorological Society*, 86, 73–88.

Žagar, N., Anderson, J.L., Collins, N., Hoar, T., Raeder, K., Lei, L. and Tribbia, J. (2016) Scale-dependent representation of the information content of observations in the global ensemble Kalman filter data assimilation. *Monthly Weather Review*, 144, 2927–2945.

Žagar, N., Andersson, E. and Fisher, M. (2005) Balanced tropical data assimilation based on a study of equatorial waves in ECMWF short-range forecast errors. *Quarterly Journal of the Royal Meteorological Society*, 131, 987–1011.

Žagar, N., Andersson, E., Fisher, M. and Untch, A. (2007) Influence of the quasi-biennial oscillation on the ECMWF model short-range forecast errors in the tropical stratosphere. *Quarterly Journal of the Royal Meteorological Society*, 133, 1843–1853.

Žagar, N., Buizza, R. and Tribbia, J. (2015) A three-dimensional multivariate modal analysis of atmospheric predictability with application to the ECMWF ensemble. *Journal of the Atmospheric Sciences*, 72, 4423–4444.

Žagar, N., Gustafsson, N. and Källén, E. (2004) Variational data assimilation in the tropics: the impact of a background error constraint. *Quarterly Journal of the Royal Meteorological Society*, 130, 103–125.

Žagar, N., Isaksen, L., Tan, D. and Tribbia, J. (2013) Balance properties of the short-range forecast errors in the ECMWF 4D-Var ensemble. *Quarterly Journal of the Royal Meteorological Society*, 139, 1229–1238.

Žagar, N., Rennie, M. and Isaksen, L. (2021) Uncertainties in kelvin waves in ECMWF analyses and forecasts: insights from Aeolus observing system experiments. *Geophysical Research Letters*, 48, e2021GL094716.

Zaplotnik, V., Žagar, N. and Gustafsson, N. (2018) An intermediate-complexity model for four-dimensional variational data assimilation including moist processes. *Quarterly Journal of the Royal Meteorological Society*, 144, 1772–1787.

How to cite this article: Li, L., Žagar, N., Raeder, K. & Anderson, J.L. (2023) Comparison of temperature and wind observations in the Tropics in a perfect-model, global EnKF data assimilation system. *Quarterly Journal of the Royal Meteorological Society*, 149(755), 2367–2385. Available from: https://doi.org/10.1002/qj.4511